Journal of Research and Applications in Mechanical Engineering
ISSN: 2229-2152 (Print); 2697-424x (Online)
(2025) Vol. 13, No. 2, Paper No. JRAME 25-13-018
[DOI: 10.14456/jrame.2025.18]

Research Article

Numerical Simulation of Harmonic Gust Induced 2D Low-Re Incompressible Flow Over Tandem Circular Cylinders using ECFRUNS

Y. A. Joshi[1,*]
R. Bhoraniya[2]
A. B. Harichandan[3]
[1] *Department of Mechanical Engineering, GEC Rajkot, Technical Edu. Department, Rajkot 360005 Gujarat, India*
[2] *Department of Mechanical Engineering, Faculty of Engineering at Marwadi University, Morbi Highway, Rajkot 360003, India*
[3] *Department of Mechanical Engineering, Centre for UG and PG studies (CUPGS), Biju Patanayak University of Technology, Raurkhela 769015, Odisha, India*

Received 26 July 2024
Revised 1 October 2024
Accepted 10 October 2024

Abstract:
The paper presents a numerical investigation of the harmonic gust induced two dimensional incompressible flow over two tandem circular cylinders configurations. The extended cell flux reconstruction scheme (ECFRUNS), developed for unstructured triangular cells grid, have been employed for the flow solution. The gust angular frequency (ω), which is the variable generating impulse harmonic gust and affecting inlet flow fluctuations, has been investigated to identify its effective value for improved qualitative wake characteristics. The low- Reynolds number (Re) as a second flow variable has been investigated with an impulse harmonic (gusty) inflow to examine the effect of the Reynolds number under gusty situations. The non-dimensional longitudinal gap-to-diameter ratio (R = L/D) as a geometrical variable has also been investigated to check its effect with a combination of flow variables and gust. The streamlines and vorticity contours are employed for quantitative flow visualization. The force coefficients (C_l & Cd), and the Strouhal Number (St) have been computed as quantitative result parameter. They are compared with literature wherever possible. The investigated flow characteristics i.e. vortex shedding frequency, gap flow, wake region have been discussed in detail. The investigations establishes the capabilities of ECFRUNS scheme to solve one dimensional harmonic gust induced low-Re incompressible external flow problems explicitly directly on physical plane.

Keywords: *Low-Re, gust frequency, incompressible flow, circular cylinders, wake, vorticity*

1. Introduction

The concern about continuous advancement in computational fluid dynamics and its solution approaches has been one of the main thrust areas of research amongst the scientific community. There are two basic approaches to solution: implicit and explicit. The implicit schemes are widely accepted because they can handle complex equations. But implicit scheme not only demand high order computer requirements but also they have limitations to capture flow characteristics specifically in separated flow region [1]. Roy and Bandyopadhyay [2] introduced a novel technique known as consistent flux reconstruction (CFR). This technique incorporates explicit calculations for both the reconstruction of flux at the cell face center and the updating of the cell center momentum equation. As a result, need for laborious matrix inversion operations has been eliminated. The computational technique described in the study conducted by Omprakash et al. [3] was utilized for the analysis of flow characteristics around a wedge. Harichandan and Roy [1] extended CFR technique and introduced consistent flux reconstruction for unstructured triangular grid (CFRUNS).

---

[*] Corresponding author: Y. A. Joshi
E-mail address: eryagnesh@gmail.com

It could solve flow past problems with unstructured triangular grid. In their study, they reported low and high Reynolds number incompressible uniform flow past cylinders and airfoils. This study exhibits the capabilities of ECFRUNS to predict flow physics phenomena in separation zone for uniform harmonic inflow (gusty) cases of the fluid flow. The literature review about flux reconstruction also suggest that, the method with flux reconstruction has batter computational efficiency compared to the similar method without cell flux reconstruction

The problem of flow over cylinders is under intense research due to its wide range of applications in the field of engineering. The harmonic inlet flow (Gusty flow) is a special case of flow under the effect of which the structure exhibits unique behavior. Several researchers have reported investigations based on gusty flow. Richard and Donely [4] reported study of gust for airplanes. They reported that the gust frequencies can be helpful to predict stress frequencies in the primary structures of airplanes. Bullen [5] reported the data about variation of gust frequency with gust velocity, and variation of gust frequency with altitude. He presented this data in graphical manner that can be used for estimation of damage fatigue due to gust load. Narita and Katsuragi [6] reported wind tunnel experimental study and field observation study about gust wind characteristics near Yoneyama Bridge. They investigated gust wind affect about a reference case of vehicle under the effect of local topographical condition and vehicle safety. A benchmark problem of the single airfoil gust response for wide range of gust frequencies reported by J R Scott [7]. The study also compares the results with classical problem of flat plate. The report concludes the effect of geometry on far-field acoustic intensity and airfoil unsteady pressure. Golubev et al. [8] developed a highly precise tool for predicting fluid-structure interaction phenomena. They created an efficient model to incorporate unsteady incompressible 2D vertical flow perturbations within the computational domain by adding a source term in the momentum equations. Their study focused on the behavior of stationary and pitching airfoil sections exposed to unsteady viscous flow with harmonic gusts, validating their results through comparisons with experimental data and previously verified numerical predictions. In a follow-up study, Golubev et al. [9] extended their model to include viscous effects and analyzed the responses of a Joukowski airfoil to vertical gusts. Bryja [10] introduced a method for evaluating buffeting responses in numerical studies of suspension bridge dynamics under fluctuating winds. This technique involved adding an additional periodic component to the mean wind velocity function, which is typically assumed to be steady, aligning with the natural frequency of bridge vibrations. This component simulates a series of repetitive wind gusts. Afgan et al. [11] investigated the fluid flow moving on a flat plate at a Reynolds number of 750 using a refined large-eddy simulation (LES) technique. Their study aimed to provide insights into the flow characteristics and turbulence behavior at this Reynolds number. The results align with both direct numerical simulation and experimental evidence, confirming the accuracy of the simulations. The study also examines the standard flat plate subjected to an incoming gust signal and compares the findings to simulations with a constant inlet flow. The study examines the reaction of a flat plate to 16 distinct gust patterns. It presents a method for reconstructing the transient drag in these circumstances. Ginger et al. [12] examined the utilization of peak gust wind speeds in the fields of building design. This text examines the source of the fundamental maximum gust speed in the Australian Wind Loading Standards, which has been determined using the Dines anemometer since 1971. The reactivity of the Dines anemometer to gusts is contrasted with the recording technology of Automatic Weather Stations (AWS), which registers lower gust velocities. The report also presents a technique for comparing gust wind velocities and harmonizing wind data with other standards.

Kraniotis et al. [13] found that wind-driven air infiltration significantly contributes to energy loss in buildings, negatively affecting energy efficiency. The study examined the impact of wind gustiness on water infiltration in a low-rise building. The simulation included two levels of gust frequency and a ratio, representing seven cases of exterior leakage distribution and five scenarios of compartmentalization and internal leakages. The findings showed a positive correlation between increased wind gustiness and greater air exchange rates, emphasizing the importance of accurately identifying exterior leakages and implementing internal leakage control to minimize infiltration rates. Yi Liu et al. [14] conducted a study on the nonlinear aeroelastic response of a flexible wing with a large aspect ratio, activated by a harmonic gust load. They used a combination of numerical calculations, structural dynamic analysis, and non-planar unstable vortex lattice aerodynamic computation to model the wing's reaction to gust load. The results showed satisfactory quantitative agreement, suggesting the technique is suitable for forecasting flexible wings' geometrically nonlinear gust response. Ladinek et al. [15] performed an experimental investigation on the flow behavior around an Ahmed body under yawing conditions. The study considered two slant angles, 25° and 35°, and involved Reynolds numbers reaching up to 2.784 × 10^6. The study specifically examines the effects of crosswinds on aerodynamics. Yawing angles have a substantial impact on forces and moments, particularly on lift and pitching moment. These variables experience pronounced variations because of bi-stable flow occurring at a crucial angle. PIV measurements are employed to analyze and elucidate the temporal patterns of forces and moments. Suder and Sarkar [16] conducted a study to assess the efficacy of experimentally derived coefficients in forecasting aerodynamic loads on a blade under varying wind conditions. The study performed independent experiments on a scaled-up blade section model in a wind tunnel, utilizing measured loads (lift and moment) to verify simulated loads. A refined loads model was created by incorporating an extra lag term, demonstrating its performance in scenarios of smooth, gusty, and turbulent wind. Rana et al. [17] performed a study on the fluid flow around a circular cylinder undergoing rotation to investigate its response to gusts. They examined uniform flow and heat transfer characteristics at low Re. By investigating seven different gust profiles, they observed how gusty inflow affected vortex detachment and convection.

Zhan et al. [18] utilized the FLUENT commercial software to analyze the energy efficiency of a partially activated flapping foil in gusty airflow. This foil, rotating around an axis at one-third of the chord length, underwent vertical motion due to lift force. Unlike previous studies, they considered an unstable flow with a cosine velocity profile. Their investigation, conducted at a Reynolds number of 1100, studied various mechanical parameters and found that windy flow increased energy harvesting potential, with efficiency improving with gust fluctuations. Bali and Supradeepan (2019) [19] presented an Arbitrary Lagrangian-Eulerian (ALE) an incompressible finite volume method utilizing the Consistent Flux Reconstruction approach. This scheme was employed to investigate 2-D incompressible viscous flow around a cylinder undergoing both rotation and transverse oscillation. Their study focused on the formulation and verification of the ALE-CFR scheme, followed by practical application. By adjusting the frequency ratio, they varied the transverse oscillation frequency relative to the natural Strouhal frequency, enabling the investigation of vortex shedding characteristics and the influence of rotational and transverse oscillations on lift and drag. AB Harichandan et al [20, 21] reported investigations for gusty flow over side-by-side and staggered cylinders. Gajula et al. [22] conducted a study on airflow around a circular cylinder using ANSYS Fluent and numerical simulations. The study aimed to examine the development of aerodynamic forces at different Reynolds numbers and gust frequency. The study found that gusts are induced by varying the direction of incoming velocity at different frequencies, releasing vortices simultaneously from both upper and lower surfaces of the cylinder. The levels of $C_{l,}$ C_d, and Strouhal number increased with gust frequency, regardless of Reynolds number. Fast Fourier transform analysis was used to investigate the energy spectrum and kinetic energy contours of vorticity and turbulence. The findings provide a deeper understanding of gust flow and circular cylinder dynamics. The study also assessed the efficacy of empirically derived factors in forecasting aerodynamic forces on a blade under varying wind conditions.

Through the literature review, it has been noticed that (1) out of two main CFD solution approaches, implicit and explicit, the first is adopted a lot due to its capability of faster solution and versatility. The explicit approach is under-attended despite its simplicity and capacity to capture specific flow features. There is an opportunity to extend explicit schemes for applications like gusty flow where it can serve better. The gusty flow have several applications in field of engineering It can applied to prediction of the vortex induced vibrations in structures like bridges, off sour platforms etc. Apart from these applications, there are the applications where the study about gusty inflow over cylinder could be helpful for heat transfer enhancement, turbulence modulation, analysis sound generation too. (2) The low-*Re* flow investigations reported for flow with harmonic inflow were limited even though its wide range of applications in different area of engineering. Considering research gap (1) and (2), and to make numerical results comparable with the literature results of uniform flow over similar geometry, the low Reynolds number values and non-dimensional gap to diameter ratios are directly selected based on literature without conducting design of experiments.

In view of all above the numerical investigation on harmonic gust induced two dimensional incompressible flow over two tandem circular cylinder configurations have been attempted using extended cell flux reconstruction scheme (ECFRUNS), developed for unstructured triangular cells grid.

2. Geometric description and numerical consideration

The geometric arrangement of two circular cylinders with equal diameters D positioned in tandem, with a longitudinal gap L measured from center to center, is illustrated in Fig. 1. The top and bottom boundaries are placed at transverse distance of 10 times D reference to centerline to ensure that the blockage ratio remains below 10% for various multi-cylinder configurations. The inflow boundary is also set at 10 x D from center of front cylinder, while outflow boundary is positioned 25 x D downstream from center of rear cylinder.

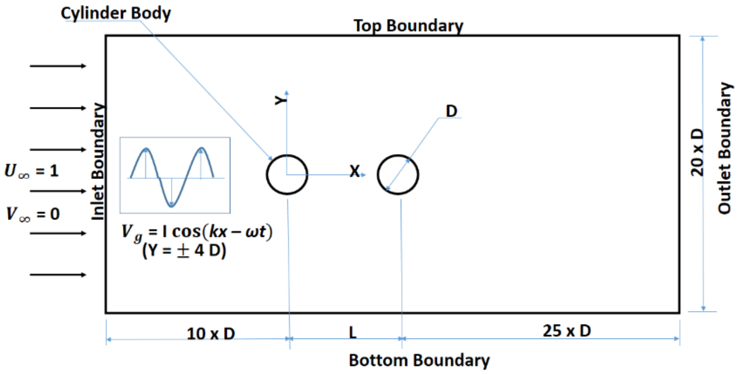

Fig. 1. Schematic of two tandem cylinders under gusty flow.

Before proceeding with the simulation, several physical and numerical considerations were addressed. Free-stream Dirichlet boundary conditions were employed at all outer boundaries, while no-slip condition was used on cylinder surfaces. Various gust frequencies (0.2π, 0.5π and π) and flow Reynolds numbers (50, 75 and 100) were considered, along with different longitudinal gap-to-diameter ratios (1.5, 2 and 3). Simulations for all possible combinations were conducted using a time step of 0.001 seconds. The numerical solutions were obtained at $t_{non\text{-}dimensional} = 100$ to ensure convergence. The resulting simulation data were then analyzed to provide detailed insights into the flow characteristics, specifically focusing on aerodynamic force coefficients and shedding frequencies are presented here.

A region within inlet is designated, and a perturbation velocity component in v-direction is added to uniform flow. To accommodate this perturbation while maintaining incompressibility constraint, a source term is added in to momentum equation. The governing equations associated with flow investigation as mentioned above incorporate this source terms. The heat transfer and body forces are neglected. The crosswise perturbation velocity component used to generate gust can be expressed as follows:

$$v_g = I\cos(kx - \omega t) \tag{1}$$

here $I = I_g \times U_\infty$, I represents gust intensity, I_g represents gust intensity relative to the mean flow, U_∞ represents free-stream velocity, ω represents angular gust frequency, and k represents gust wave number. Two related parameters are defined as linear gust frequency $f = \frac{\omega}{2\pi}$, and imposed gust reduced frequency $f_i = \frac{\omega D}{2U_\infty}$.

A disturbance, as discussed above, is introduced through inlet boundary, as demonstrated in Fig. 1, which is liable for generating the v- perturbation velocity component. This source is positioned within uniform flow and aligned with flow direction. To reduce wave reflections and distortions in the flow, which may arise when the perturbation field fails to satisfy the incompressibility constraint, gust source is incorporated as source term in y-momentum equation. These approach for gust problem solution was introduced by Golubev et al. [23]. The gust source S_v must comply below equations:

$$\frac{\partial v_g}{\partial t} + U_\infty \frac{\partial v_g}{\partial x} = S_v \tag{2}$$

$$\frac{\partial S_v}{\partial y} = 0 \tag{3}$$

In the current computations, initial values equal to free-stream pressure and u-velocity have been allocated to every triangular cell within domain. A zero free-stream v-velocity is assigned to each cell throughout region, except for those located within gust source region.

3. Governing Equation (GE) and Methodology of solution

The equations that describe two-dimensional, incompressible, viscous fluid flow consist of continuity equation and momentum equations. These have been reformulated in conservative, non-dimensional primitive variable form, without considering body forces or heat transfer components, as follows:

Continuity equation:

$$\frac{\partial u}{\partial x}+\frac{\partial v}{\partial y}=0 \tag{4}$$

Momentum equations:

(1) x-momentum:

$$\frac{\partial u}{\partial t}+\frac{\partial\left(u^2\right)}{\partial x}+\frac{\partial(uv)}{\partial y}=-\frac{\partial p}{\partial x}+\frac{1}{Re}\times\left(\frac{\partial^2 u}{\partial x^2}+\frac{\partial^2 u}{\partial y^2}\right) \tag{5}$$

(2) y-momentum:

$$\frac{\partial v}{\partial t}+\frac{\partial(uv)}{\partial x}+\frac{\partial\left(v^2\right)}{\partial y}=-\frac{\partial p}{\partial y}+\frac{1}{Re}\times\left(\frac{\partial^2 v}{\partial x^2}+\frac{\partial^2 v}{\partial y^2}\right) \tag{6}$$

In this framework, the velocity components u and v correspond to the flow velocities in x and y directions, respectively. The variable p represents the pressure-to-density ratio. Non-dimensional time (*t* = *t*_dimensional × U∞/L) is expressed as the product of dimensional time and the ratio of free-stream velocity to a characteristic length scale of the flow problem.

In the application of the ECFRUNS solver, initial values for pressure and velocity at each triangular element in the computational domain are set to the free-stream values. This represents the scenario where cylinder is suddenly introduced into flow stream. At inlet of computational domain, Dirichlet boundary conditions are applied for both pressure and velocity, while Neumann boundary conditions are used at other boundaries. Additionally, no-slip condition is enforced on cylinder surface.

To achieve a solution numerically, GEs are discretized using FVM, which relies upon their integral form. GEs are integrated over discrete finite volumes to derive the solution, requiring only the coordinates of the cell corners for this process. For a given triangular cell, depicted in Fig. 2(a), the continuity and momentum equations are integrated over the two-dimensional domain.

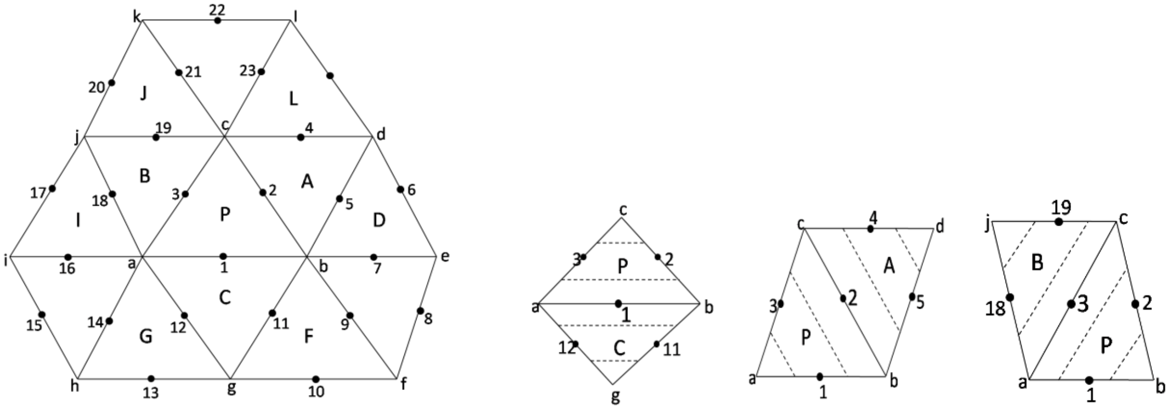

(a) (b)

Fig. 2. Schematic of two tandem cylinders under gusty flow (a) ECFRUNS stencil of triangular control volume (b) Reconstruction of control volumes

ECFRUNS solver uses a cell-centred grid configuration, where u, v and p are considered at cell centers. To compute fluxes across each cell face, it is necessary to determine cell face centres values of u1, u2, u3, v1, v2, v3, p1, p2 and p3. This is achieved using consistent flux reconstruction scheme based on triangular cells. Momentum equations are solved to obtain face center velocities of each reconstruction cell. Poisson equation for pressure is then derived by substituting these values into discretized continuity equation. Solving pressure-Poisson equation yields pressure values at cell centers, which are then linearly interpolated to determine cell face center pressure.

The current solver employs a completely explicit approach to reconstruct cell face centre velocities and update cell centre variables. Both pressure and velocity computations utilize a 10-point stencil. Figure 2(b) depicts the flux reconstruction cells at cell face centers '1', '2' and '3'. The solver is second order in space and time accurate. The discretization of GEs with consideration of flux reconstruction as explained below:

The x-momentum equation:

Unsteady term:

$$\iint\limits_{S_1} \left(\frac{\partial u}{\partial t}\right)_1 dS_1 = \left(\frac{\partial u}{\partial t}\right)_1 A_1 = \left(\frac{3u_1^{n+1} - 4u_1^{n} + u_1^{n-1}}{2\Delta t}\right) \times \left(A_P + A_C\right) \tag{7}$$

Convective terms:

$$\begin{aligned}
&\iint\limits_{S_1} \left(\frac{\partial (uu)}{\partial x} + \frac{\partial (vu)}{\partial y}\right)_1 dS_1 = \oint\limits_{C_1} \left((uu)\times dy - (vu)\times dx \right) \\
&= u_{11}^2 \times \Delta y_{gb} - u_{11} \times v_{11} \times \Delta x_{gb} + u_2^2 \times \Delta y_{bc} - u_2 \times v_2 \times \Delta x_{bc} \\
&+ u_3^2 \times \Delta y_{ca} - u_3 \times v_3 \times \Delta x_{ca} + u_{12}^2 \times \Delta y_{ag} - u_{12} \times v_{12} \times \Delta x_{ag} \\
&+ O(|r_{12}|^3, \ldots\ldots) = UCFLUX_1
\end{aligned} \tag{8}$$

Pressure terms:

$$\begin{aligned}
&\iint\limits_{S_1} \left(\frac{\partial p}{\partial x}\right)_1 dS_1 = \oint\limits_{C_1} p dy = p_{11} \times \Delta y_{gb} + p_2 \times \Delta y_{bc} + p_3 \times \Delta y_{ca} + p_{12} \times \Delta y_{ag} \\
&= UPFLUX_1
\end{aligned} \tag{9}$$

Diffusive terms:

$$\begin{aligned}
&\iint\limits_{S_1} \left[\frac{\partial}{\partial x}\left(\frac{\partial u}{\partial x}\right) + \frac{\partial}{\partial y}\left(\frac{\partial u}{\partial y}\right)\right]_1 dS_1 = \oint\limits_{C_1} \left[\left(\frac{\partial u}{\partial x}\right) \times dy - \left(\frac{\partial u}{\partial y}\right) \times dx\right] \\
&= \left(\frac{\partial u}{\partial x}\right)_{11} \times \Delta y_{gb} + \left(\frac{\partial u}{\partial x}\right)_{2} \times \Delta y_{bc} + \left(\frac{\partial u}{\partial x}\right)_{3} \times \Delta y_{ca} + \left(\frac{\partial u}{\partial x}\right)_{12} \times \Delta y_{ag} \\
&- \left(\frac{\partial u}{\partial y}\right)_{11} \times \Delta x_{gb} - \left(\frac{\partial u}{\partial y}\right)_{2} \times \Delta x_{bc} - \left(\frac{\partial u}{\partial y}\right)_{3} \times \Delta x_{ca} - \left(\frac{\partial u}{\partial y}\right)_{12} \times \Delta x_{ag} \\
&+ O(|r_{12}|^3, \ldots\ldots) = UDFLUX_1
\end{aligned} \tag{10}$$

When evaluating the transient term, the flux value for reconstruction cell is determined based on the value of the variable at its center. In the equations (1.6 – 1.9), S_1 refers to the reconstructed domain and C_1 represents the boundary that encloses it. To compute viscous fluxes on face '1', velocities at locations 'a', 'g', 'b' and 'c' are required. These values are estimated by linearly interpolating the property values of neighboring cell centers. The equation utilized to calculate the nodal value at 'a' can be expressed as:

$$\phi_a = \frac{\sum_i \left(\frac{\phi_P[i]}{d[i]}\right)}{\sum_i \left(\frac{1}{d[i]}\right)} \tag{11}$$

In the given context, the variable Φ[i] represents the value at the center of any neighboring cell of node 'a'. d[i] represents the distance between and node 'a' and the center of the neighboring cell. The number of neighbors (i) can vary depending on the specific node. Using the eq. 1.6 – 1.9, we can derive equation for u1 which can be expressed at (n+1)th time level as follows:

$$u_1^{n+1} = \frac{4}{3}u_1^{n} - \frac{1}{3}u_1^{n-1} + \frac{2\Delta t}{3(A_P + A_C)} \times \left(-UCFLUX_1 - UPFLUX_1 + \left(\frac{1}{Re}\right) \times UDFLUX_1 \right) \tag{12}$$

At the nth time level, the cell face velocity is calculated by linearly interpolating the values of neighboring cell centers at that specific time level. Likewise, other velocities at next time level are determined.

Nevertheless, there is no need for cell-face velocity reconstruction of cylinder surface cells because no-slip condition is enforced on those faces. But, during reconstruction for remaining two faces, meticulous computations have been carried out to ensure that no-slip condition is satisfied at all nodal points along the body surface. The pressure values at body surface are determined by using neighboring points in the flow field, while enforcing a condition of zero pressure gradient in the normal direction. Body surface velocity derivatives are determined by introducing a pseudo cells layer underneath cylinder surface, where the variables possess same absolute value with opposite sign compared to corresponding value on cylinder surface.

Pressure-Poisson equation:

By substituting expressions for various variables into discrete continuity equation, the resulting Pressure-Poisson Equation can be expressed as follows:

$$p_P = \frac{1}{C_P} \times \begin{bmatrix} \left(\frac{1}{2} \times SOURCE\right) - C_A \times p_A - C_B \times p_B - C_C \times p_C - C_D \times p_D \\ -C_F \times p_F - C_G \times p_G - C_I \times p_I - C_J \times p_J - C_L \times p_L \end{bmatrix} \tag{13}$$

In this equation, the geometrical coefficients (C_i) represent the discrete cell and its neighboring cells, the cell pressure values have been represented by term p_i.

The detail understanding about solution methodology is presented through flow chart shown below:

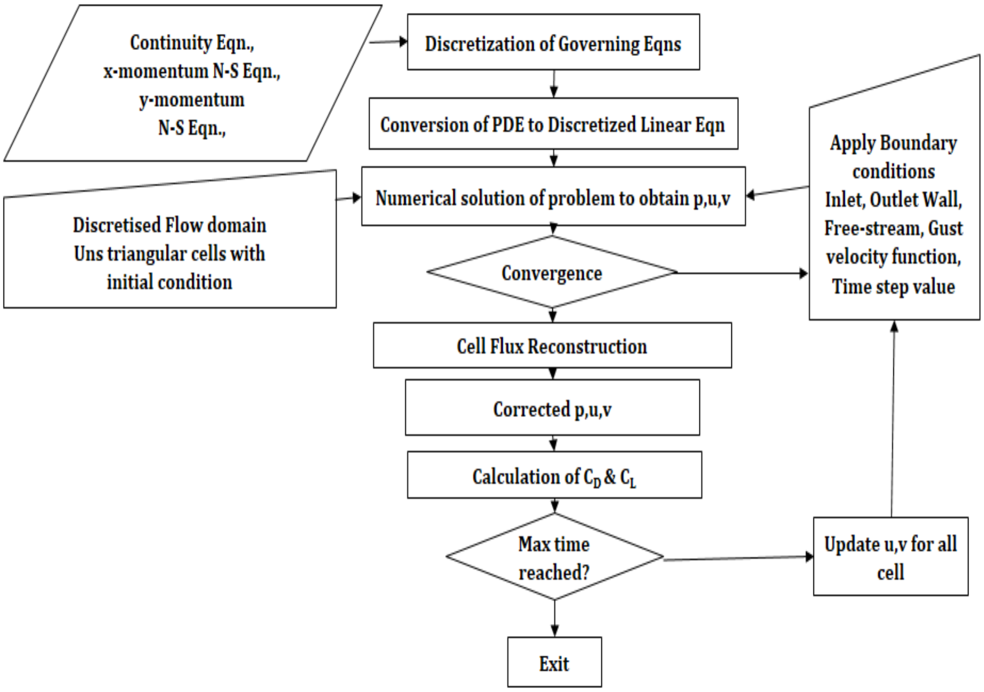

Fig. 3. Iterative Solution Methodology Flow Chart.

3. Solver validation and Convergence

3.1 Grid independence

Numerical findings for the uniform flow over an unconfined cylinder are primarily used to validate the accuracy of the ‘ECFRUNS’ solver. A grid independence analysis was performed using four different grids, each varying in the number of nodes on cylinder's surface, to determine appropriate grid size. Table 1 represents data from grid independence analysis conducted at a Reynolds number (Re) of 100.

Table 1: Grid independence assessment for uniform flow over unconfined circular cylinder (Re = 100).

	Grid Type	C_d	C_l	***St***
1	80 nodes on cylinder surface	1.108± 0.021	± 0.161	0.168
2	120 nodes on cylinder surface	1.165 ± 0.015	± 0.192	0.164
3	160 nodes on cylinder surface	1.225 ± 0.010	± 0.21	0.161
4	200 nodes on cylinder surface	1.238 ± 0.010	± 0.223	0.161

After evaluating the variations in the Strouhal number, lift coefficients, and drag coefficients, Grid 3 was selected for the flow computations due to its successful performance. The grid chosen based on the grid convergence analysis for simulating flow at Reynolds number of 100 also adheres to ASME (2008) recommended grid convergence index (GCI). The pressure-Poisson equation employed to calculate the pressure. The convergence condition is adjusted at each time level to ensure that simulation residual remain near $10^{(-6)}$.

3.2 Results Verification with published data for uniform flow over cylinder

The experimental data from the literature is compared with the current numerical results computed for uniform flow over single cylinder problem. Figure 4(a) shows a comparison of drag coefficients. The experimental results from Weisenberger [24] and Tritton [25] are generally lower than our numerical values. For further comparison, the numerical data from Gresho et al. [26] is also included. It is found that the values from the current numerical model fall between the experimental results cited here.

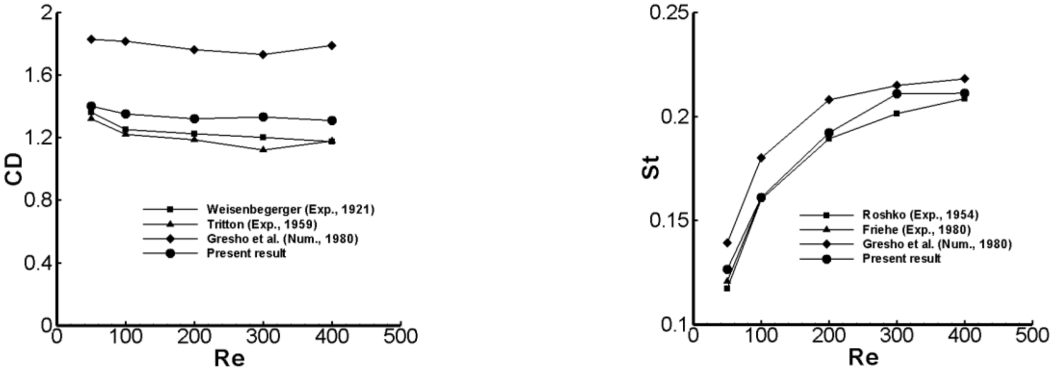

(a) (b)

Fig. 4. Comparison between experimental and current numerical results for uniform flow over single cylinder.

In Fig. 4(b), a comparison is made between the Strouhal number obtained from our numerical simulation and the experimental results of Roshko [27] and Friehe [28]. There is a satisfactory agreement between our numerical values and the experimental data, though our numerical values are slightly higher. The deviation between the experimental results and our findings for drag coefficient and Strouhal number can be attributed to two potential factors. This may be due to absence of three-dimensional effects, and coarser grid used downstream of cylinder in present simulation. This demonstrates the successful establishment of our numerical scheme ECFRUNS for flow over bluff bodies like cylinder. With this confidence, ECFRUNS scheme have also been extended to gusty flow over circular cylinder to gain further insights of flow characteristics.

Table 2 displays the average and amplitude of C_l and C_d, as well as St, comparing our results with other published numerical findings. Notably, our results align well with those from other studies.

Table 2: Comparison of output flow variables for single circular cylinder.

Flow Variables	*Re* = 100			*Re* = 200		
	C_d	C_l	*St*	C_d	C_l	*St*
Wiesenberger [24]	1.326 ± 0.01	--	0.1608	--	--	--
Tritton (1959) [25]	1.32 ± 0.01	--	0.16	--	--	--
Gresho et al. [26]	1.816 ± 0.01	--	0.18	--	--	--
Braza et al. [29]	1.364 ± 0.015	± 0.25	0.16	1.40 ± 0.05	± 0.75	0.2
Meneghini et al. [30]	1.37 ± 0.01	--	0.165	1.30 ± 0.05	--	0.196
Ding et al. [31]	1.356 ± 0.01	± 0.287	0.166	1.34 ± 0.05	± 0.659	0.196
Roy et al [1]	1.352 ± 0.01	± 0.278	0.161	1.32 ± 0.05	± 0.602	0.192
Present Result	1.225 ± 0.01	± 0.21	0.161	1.28 ± 0.01	± 0.501	0.191

4. Results and Discussion for gusty flow over two tandem cylinders

The grid independence test for the computational domain in case of gusty flow past multiple cylinders has not been carried out explicitly. Rather, the simulations in present cases are carried out with 160 numbers of nodes on each cylinder surfaces as have been concluded from grid independence test upon single circular cylinder, as the adopted level of fineness found capable to capture flow separation adequately. Computational grid for three different cases with R = 1.5, 2 and 3 are depicted in Fig. 5. The aerodynamic force coefficients and Strouhal statistics are calculated and then compared for detailed analysis. The numbers of flow domain element in all three configurations are in the range of 32000~40000.

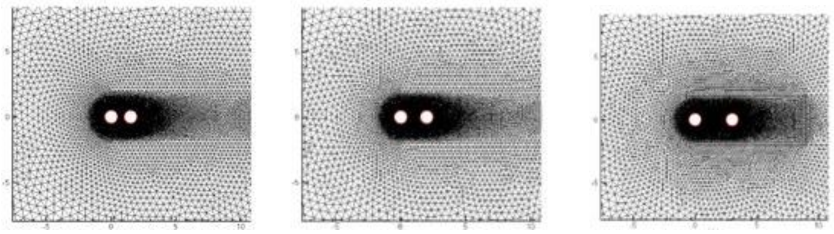

Gap ratio, R = 1.5 Gap ratio, R = 2 Gap ratio, R = 3

Fig. 5. Computational domain for cylinders in tandem configuration.

The details of computational grid mesh used in present scenario are presented in Table 3 as shown below.

Table 3: Grid details of flow domain of cylinders in tandem.

Triangular Mesh Type	**Geometric description**	**No of elements**	**No of nodes**
1	R = 1.5	32860	16653
2	R = 2.0	34848	17651
3	R = 3.0	39524	19979

Figure 6 displays vorticity and streamline contours of gusty flow over tandem cylinders with *Re* = 50 and $\omega = 0.2\pi$ for three different gap ratios at $t_{\text{non-dimensional}} = 100$. For lower gap ratio, it has been noticed that flow gets restricted between the cylinders as shear layer from upstream cylinder reattaches to shear layer from downstream cylinder. For R = 2, it has been noticed that a steady vortex is formed in longitudinal space between cylinders. This vortex is formed primarily due to flow separation on back of the upstream cylinder.

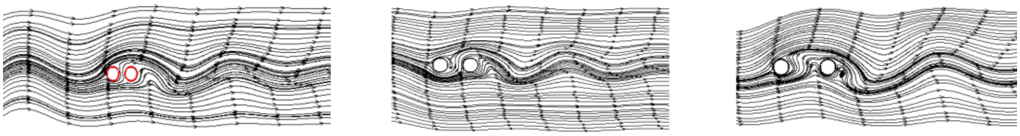

Streamline Contours

Vorticity Contours

Gap ratio, R = 1.5 Gap ratio, R = 2 Gap ratio, R = 3

Fig. 6. Flow contours for tandem cylinders at *Re* = 50, ω = 0.2π.

This steady vortex also seems to reattach with the shear layers on front of the downstream cylinder. However, for larger longitudinal space, R = 3, upstream cylinder shedding vortex tend to escape from the intermediate space and move over the downstream cylinder alternately. This, in turn, interacts with the shedding vortices from downstream cylinder, and forms a wider wake of greater strength.

Figure 7 displays the time-dependent aerodynamic force coefficients experienced by both the cylinders at *Re* = 50 and ω = 0.2π. Non-zero lift coefficients for both the cylinders have been observed due to superimposition of gust component on the uniform flow. However, the amplitude of lift fluctuation has been noticed to be considerably lower for front cylinder as compared to the downstream cylinder. This happens particularly due to intense interaction of shed vortices and shear layers of downstream cylinder. Harmonic fluctuation of lift coefficients is observed whereas fluctuations of drag coefficients are noticed to be semi-harmonic.

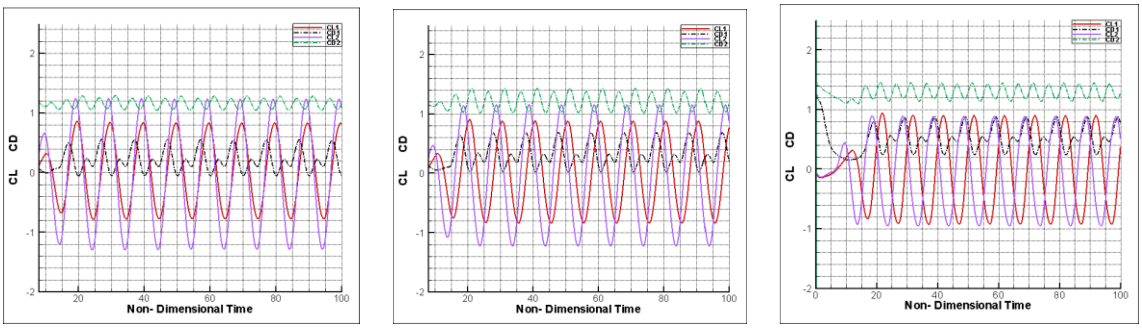

Gap ratio, R = 1.5 Gap ratio, R = 2 Gap ratio, R = 3

Fig. 7. Temporal C_l and C_d for tandem cylinders at *Re* = 50, ω = 0.2π.

The harmonic fluctuations in lift coefficient are likely due to the direct, periodic influence of the gust on the asymmetrical flow around the cylinder. In contrast, the bi-harmonic fluctuations in the drag coefficient arise from complex interplay between gust frequency (ω) and the natural vortex shedding frequency, along with the additional effects of flow separation and reattachment dynamics. The downstream cylinder has been noticed to experience more drag as compared to upstream cylinder. This may be due to the wake interference from upstream cylinder, which affects the flow separation, turbulence intensity, vortex shedding, and pressure distribution around downstream cylinder. The specific gap ratio between the cylinders further modulates these effects, leading to an overall increase in drag on downstream cylinder.

Figure 8 displays the FFT analysis of time dependent C_l for both the cylinders at *Re* = 50, ω = 0.2π for gap ratios R = 1.5, 2 and 3 respectively. It has been clearly noticed that only one dominating shedding frequency is prevalent in the energy spectrum for all the cases, for both the cylinders. In absence of vortex shedding phenomena for lower R values, the single dominating frequency indicates the gust frequency (0.1). Whereas, for higher value of gap ratio, R = 3, though proper vortex shedding takes place in the downstream of rear cylinder forming a Von-Karman vortex street like structure, but shedding frequency remains same as that of gust frequency. Strouhal number, in this case, has been found to be 0.1. The difference in values is not observed due to the lower value of flow Reynolds number (*Re* = 50) considered in the present case.

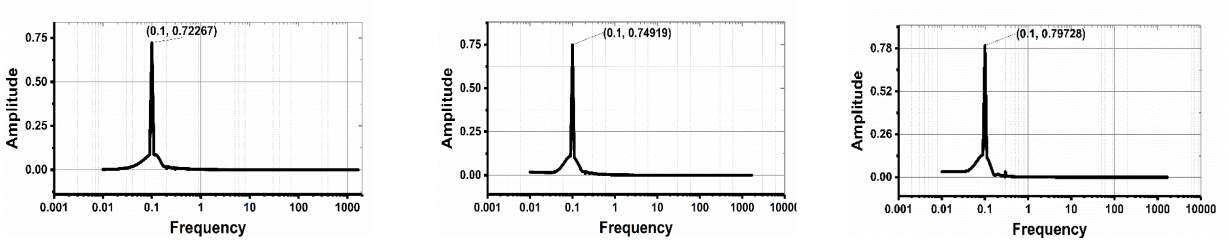

Upstream cylinder

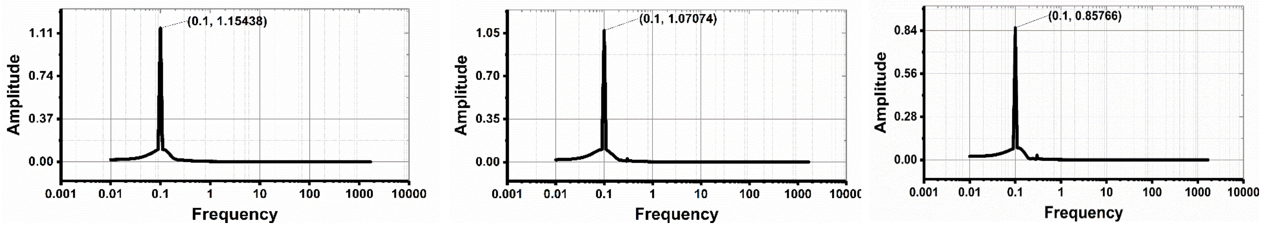

Downstream cylinder

Gap ratio, R = 1.5 Gap ratio, R = 2 Gap ratio, R = 3

Fig. 8. FFT analysis of time-dependent C_l at *Re* = 50, ω = 0.2π.

Similar investigation for *Re* = 75 and *Re* = 100 have been carried out. It has been noticed that effect of *Re* variation in range of *Re* = 50 to 100 on flow characteristics is minimal for three different gap ratios at ω = 0.2π. Therefore, further studies on gusty flow past tandem cylinders are carried out for different gap ratios for ω = 0.5π and 1.0π with *Re* =100.

Figure 9 displays vorticity and streamline contours of gusty flow over tandem cylinders with *Re* = 100 and ω = 0.5π for three different gap ratios at time $t_{\text{non-dimensional}}$ = 100. For all the gap ratios, steady vortex has been noticed at the intermediate space between two cylinders.

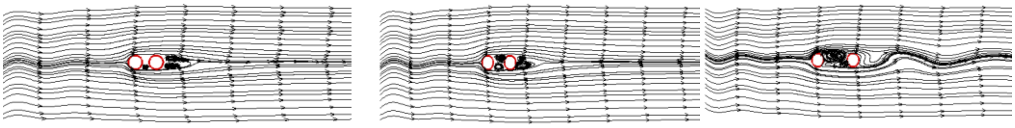

Streamline Contours

Vorticity Contours

Gap ratio, R = 1.5 Gap ratio, R = 2 Gap ratio, R = 3

Fig. 9. Flow contours for tandem cylinders at *Re* = 100, ω = 0.5π.

However, reattachment of shear layers in between the cylinders is not clearly visible at *Re* = 100. Steady vertex patterns are observed downstream of the rear cylinder at lower gap ratios R = 1 .5 and 2, but shedding of vertices has been noticed at R = 3, in cylinder wake. Elongated vortex patterns are noticed for at all three R.

Figure 10 displays the time-dependent C_l and C_d experienced by both cylinders at *Re* = 100 and ω = 0.5π. In all the gap ratios, a non-zero lift coefficient has been obtained for both the cylinders. Lift coefficient patterns are harmonic in nature whereas drag coefficient patterns are bi-harmonic. That is possibly due to complex shear layers interaction between cylinders. The temporal C_d value for rear cylinder is much larger than that of front cylinder because of elongated vortex patterns obtained with present flow situations.

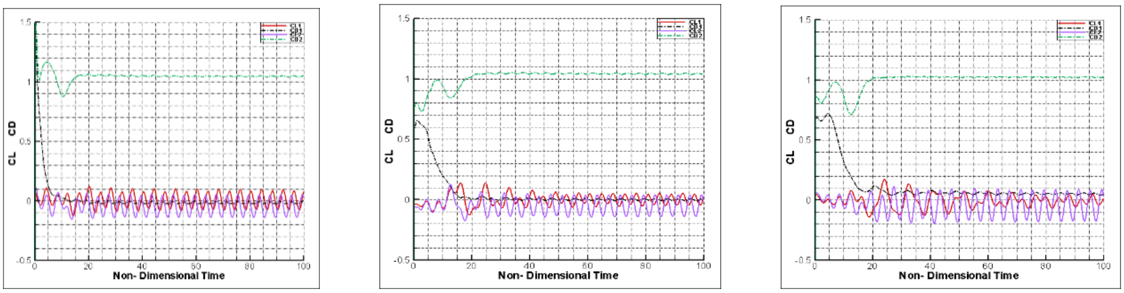

Gap ratio, R = 1.5 Gap ratio, R = 2 Gap ratio, R = 3

Fig. 10. Temporal C_l and C_d for tandem cylinders at $Re = 100$, $\omega = 0.5\pi$.

Figure 11 displays the FFT analysis of time dependent C_l for both cylinders at $Re = 100$ and $\omega = 0.5\pi$ for gap ratios R = 1.5, 2 and 3 respectively. It has been observed that for all cases of gap ratios, linear gust frequency is 0.25 as clearly mentioned in the FFT plots. However, shedding frequency in all the cases has been noticed to be less than gust frequency and the numerical value floats around 0.11~ 0.12. This is clear from the vorticity contours as shedding of vortices ceases at this gust frequency due to elongation of vortices. As reported in Chapter 3 of this thesis, Strouhal number value for uniform flow past a circular cylinder with $Re = 100$ has been 0.161 whereas it was 0.13 for gusty flow past circular cylinder with same $Re = 100$ and inlet gust frequency $\omega = 0.5\pi$. This is worth noting to mention here that in the present case, for gusty flow past two tandem cylinders under similar flow conditions, further ceasing of vortex shedding was expected and St value in the order of 0.11 ~ 0.12 justifies the involved physical phenomena.

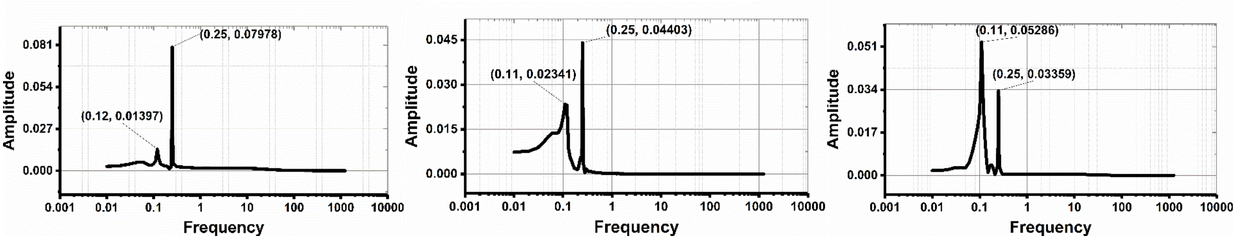

Upstream cylinder

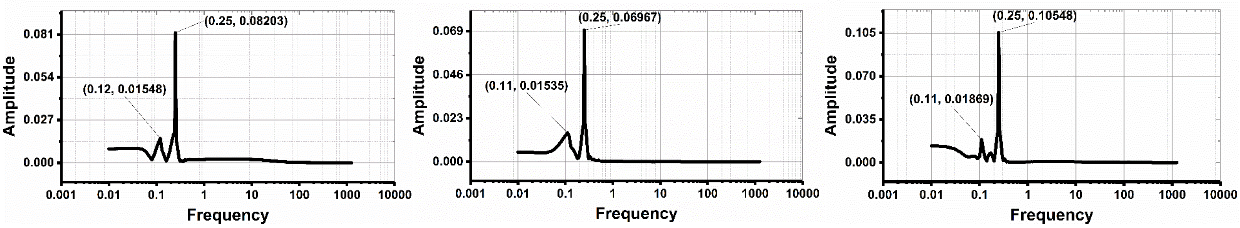

Downstream cylinder

Gap ratio, R = 1.5 Gap ratio, R = 2 Gap ratio, R = 3

Fig. 11. FFT analysis of time-dependent C_l at $Re = 100$, $\omega = 0.5\pi$.

Figure 12 displays vorticity and streamline contours of gusty flow past tandem cylinders with $Re = 100$ and $\omega = \pi$ for three different gap ratios at $t_{\text{non-dimensional}} = 100$. The streamline pattern for the gap ratios emphasizes flow separation, intense turbulence and reattachment of shear layers between the cylinders. No distinct shedding has been observed in the intermediate space between the cylinders as reattachment of shear layers occurs between cylinders. However, in the downstream of rear cylinder elongated vortex pattern has been observed for all three gap ratios.

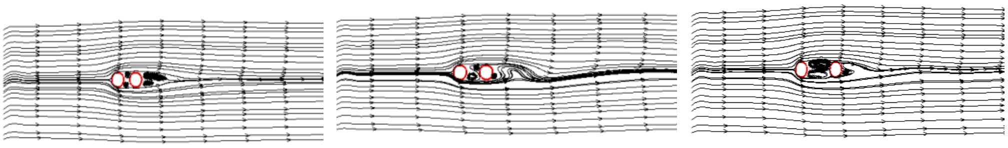

Streamline Contours

Vorticity Contours

Gap ratio, R = 1.5 Gap ratio, R = 2 Gap ratio, R = 3

Fig. 12. Flow contours for tandem cylinders at *Re* = 1000, ω = π.

Figure 13 displays the time-dependent C_l and C_d experienced by both the cylinders at *Re* = 100 and ω = π. In all the gap ratios, a non-zero lift coefficient has been obtained for both the cylinders due to inlet gust source. The complex interaction between cylinders led to harmonic lift coefficient patterns and bi-harmonic drag coefficient patterns. Because of absolute elongation of vortex pattern in the wake of rear cylinder, drag value increases drastically for rear cylinder.

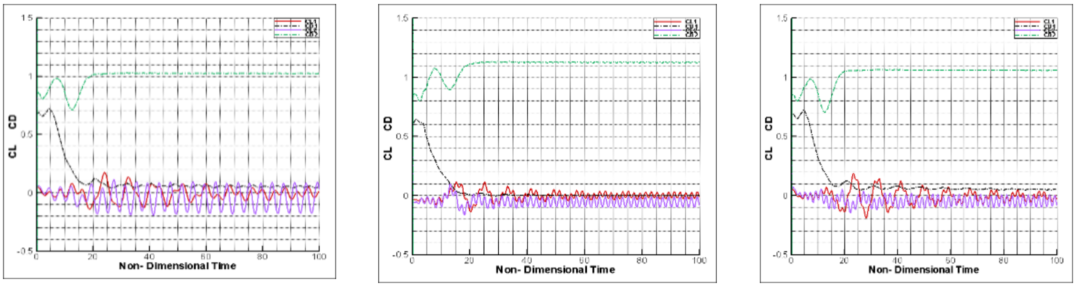

Gap ratio, R = 1.5 Gap ratio, R = 2 Gap ratio, R = 3

Fig. 13. Temporal C_l and C_d for tandem cylinders at *Re* = 100, ω = π.

Figure 14 displays the FFT analysis of time dependent C_l for both the cylinders at *Re* = 100 and ω = π for gap ratios R = 1.5, 2 and 3 respectively. It has been observed that for all cases of gap ratios, gust frequency is 0.5 as clearly mentioned in the FFT plots. However, shedding frequency in all the cases has been noticed to be less than gust frequency ranging from 0.06 ~ 0.12. This is evident from elongated vortices in the wake of rear cylinder that ceases proper shedding of vortices.

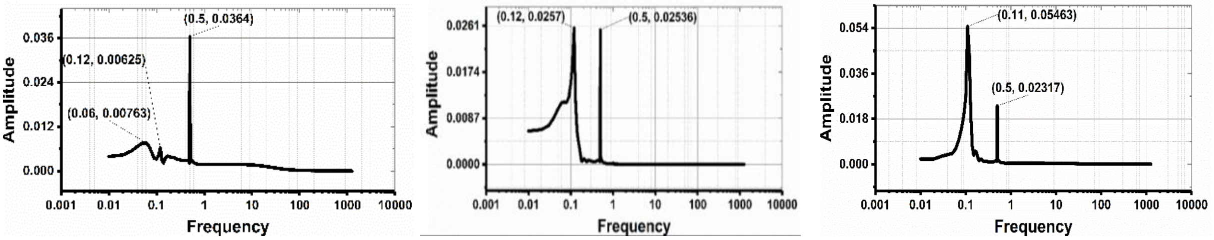

Upstream cylinder

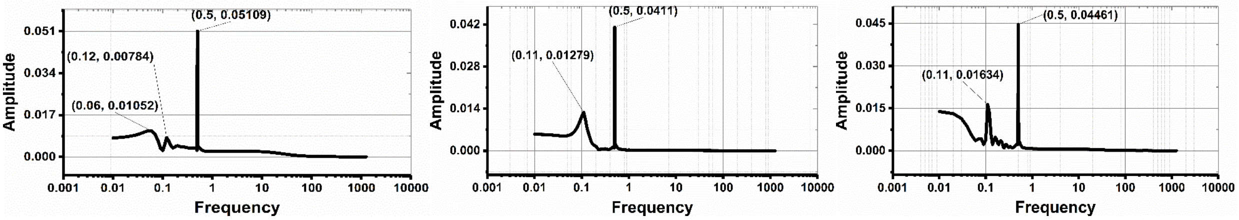

Downstream cylinder

Gap ratio, R = 1.5 Gap ratio, R = 2 Gap ratio, R = 3

Fig. 14. FFT analysis of time-dependent C_l at *Re* = 100, ω = π.

The detail comparative study of analytical and graphical data presented above have been done. The effect of variables on flow characteristics has been presented below from Fig. 15 to Fig. 16.

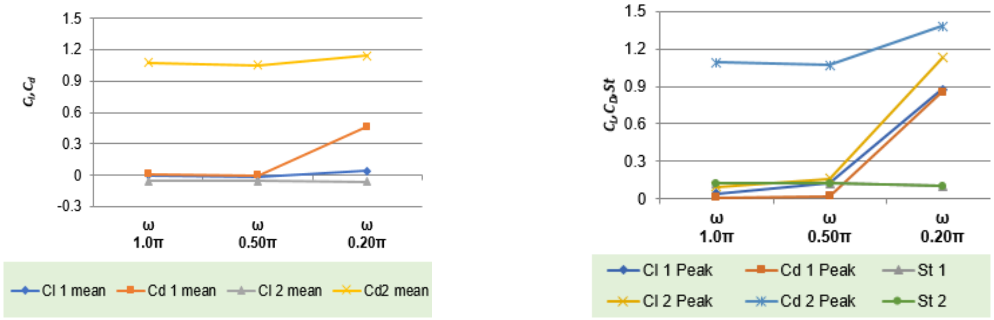

(a) (b)

Fig. 15. Effect of variation in angular gust frequency on flow characteristics.

Figure 15(a) displays the characteristics of gusty flow over two cylinders at *Re* =100 and gap ratio, R = 2 for different angular gust frequencies. The numerical values of mean C_l, mean C_d, and Strouhal number (*St*) due to variation in angular gust frequency are discussed for better understanding of flow physics. Subscripts 1 and 2 are used for front and back cylinders respectively. The values of C_l and C_d change continuously with time during a harmonic cycle of inlet gust. The fluctuation in mean value is cyclic, as observed from streamline and vorticity contours, and repeats after a particular time due to harmonic gust inlet. In Fig. 4.18, the negative value of mean lift indicates a downward lift, while the positive value indicates an upward lift. There is not a major change in the mean C_l, but the mean C_d of the upstream cylinder increases as ω varies from 1.0π to 0.2π. Figure 15(b) displays variation of peak C_d and peak C_l, along with *St* for different values of ω at *Re* = 100 and gap ratio, R = 2. It shows that the peak C_l and C_d of the front and back cylinders increase with increased inlet flow fluctuation as ω approaches from 1.0π to 0.2π. It shows that with increased inlet flow fluctuation, as ω varies from 1.0π to 0.2π, the Strouhal number for upstream and downstream cylinders slightly decreases. It falls in the range of 0.120 ~ 0.099.

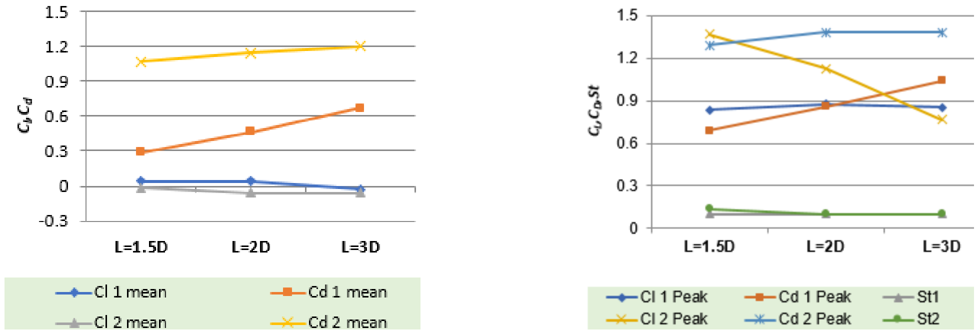

(a) (b)

Fig. 16. Effect of variation in gap ratio on flow characteristics.

Figure 16(a) displays the characteristics of gusty flow over two cylinders at *Re* = 100 and ω = 0.2π for different gap ratios (R). The mean C_l, mean C_d, and *St*, for varying R between 1.5D to 3D are presented. Subscripts 1 and 2 are used for front and back cylinder respectively. It shows that C_l and C_d for front cylinder is increasing as L/D value increases, from 1.5 to 3. The back cylinder C_l decreases while its C_d increases. Figure 16(b) represents a comparison of numerically estimated peak C_d, peak C_l, and S_t with different values of gap ratio at *Re* = 100 and ω = 0.2π. Subscripts 1 and 2 are used for front and back cylinder respectively. It shows that, for upstream cylinder 1, the peak lift slightly increases, and the peak drag remains almost same as the gap ratio increases, from 1.5 to 3. The peak C_l of the downstream cylinder decreases while its peak C_d increases. The value of *St* remains within 0.099 ~ 0.13 with the increased gap.

It can be seen, from vorticity contours comparison of cases discussed (Fig.6, Fig.9, Fig.12), that as gust frequency varies from 1.0 π to 0.2 π, the flow fluctuation increases and the alternating upper and lower flow vortices elongation decreases. It indicates increased flow mixing behind the cylinders. The streamline plot comparison also evidences that as gust frequency approaches from 1.0 π to 0.2 π, the wake area behind the cylinder is improved due to increased particle movement downstream of the cylinders.

5. Conclusion

The investigation of gusty inflow over two tandem circular cylinders has provided valuable insights into the complex aerodynamic interactions influenced by various gust frequencies, Reynolds numbers, and gap-to-diameter ratios. The simulations revealed how these factors affect the force coefficients and vortex shedding patterns, enhancing our understanding of the flow dynamics around tandem cylinders. These findings are crucial for optimizing the design and performance of structures subjected to similar flow conditions, such as bridge cables and cooling systems in power plants and many other engineering applications.

The investigations demonstrates improvement in mixing characterizes with specific gust frequency inflow. The finding could be helpful for various applications where flow mixing is the key performance i.e. chemical mixing in reactors and others. In addition, the investigations proves the capability of ECFRUNS to investigate gusty flow over tandem cylinders. It make it suitable for further investigation of various flow problems that involves harmonic inflow over structures. Through study of flow separation and reattachment can be performed that is crucial for drag reduction in various practical applications. It can applied to prediction of the vortex induced vibrations in structures like bridges, off sour platforms etc. It can also be helpful for heat transfer enhancement, turbulence modulation, and analysis of sound generation too as future scope of work.

Nomenclature

N-S	Navier-Stokes
Re	Reynolds Number
Low-*Re*	Low Reynolds Number
2D	Two-dimensional
ω	Gust angular frequencies
f	Linear gust frequencies
R	Longitudinal gap to diameter ratio
FVM	Finite Volume Method
FDM	Finite Difference Method
FEM	Finite Element Method
C_l	Coefficint of Lift
C_d	Coefficient of Drag
St	Strouhal Number
GEs	Governing Equations
Subscripts	
1	upstream circular cylinder
2	downstream circular cylinder

References

[1] Harichandan AB, Roy A. Numerical investigation of low Reynolds number flow past two and three circular cylinders using unstructured grid CFR scheme. Int J Heat Fluid Flow. 2010;31(2):154–171.

[2] Roy A, Bandyopadhyay G. A finite volume method for viscous incompressible flows using a consistent flux reconstruction scheme. 2006;m(November 2005):297–319.

[3] Omprakash P, Roy A, et al. Investigation of incompressible flow past a two dimensional wedge. J Aerosp Sci Technol. 2007;33:171–180.

[4] Rhode R, Donely P. Frequency of occurrence of atmospheric gusts and of related loads on airplane structures. Natl Advis Comm Aeronaut. 1944;L4121:1–34.

[5] Bullen NI. The variation of gust frequency with gust velocity and altitude. Minist Supply Aeronaut Res Counc Curr Pap. 1957;(1):1–19.

[6] Nobuyuk N, Masataka K. Gusty wind effects on driving safety of road vehicles. J Wind Energy Ind Aerodyn. 1981;9:181–191.

[7] Scott JR. Single airfoil gust response problem. Natl Aeronaut Space Admin. 2004;NASA-212954:45–58.

[8] Golubev VV, Dreyer BD, Golubev NV, Visbal MR. High-accuracy viscous simulations of gust interaction with stationary and pitching wing sections. 47th AIAA Aerosp Sci Meet Incl New Horizons Forum Aerosp Expo. 2009;(January):1–13.

[9] Golubev VV, Dreyer BD, Hollenshade TM, Visbal MR. High-accuracy viscous analysis of unsteady flexible airfoil response to impinging gust. 15th AIAA/CEAS Aeroacoustics Conf. 2009;(May):11–13.

[10] Bryja D. Stochastic response analysis of suspension bridge under gusty wind with time-dependent mean velocity. Arch Civ Mech Eng. 2009;9(2):15–38.

[11] Boral A, Dutta S, Das A, Kumar A, Bej N, Chaubdar P, et al. Drag reduction for flow past circular cylinder using static extended trailing edge. ASME Open J Eng. 2023;2.

[12] Afgan I, Benhamadouche S, Han X, Sagaut P, Laurence D. Flow over a flat plate with uniform inlet and incident coherent gusts. J Fluid Mech. 2013;720:457–485.

[13] Ginger J, Holmes J, Harper B. Gust wind speeds for design of structures. 2013;02(1):978–981.

[14] Kraniotis D, Thiis TK, Aurlien T. A numerical study on the impact of wind gust frequency on air exchanges in buildings with variable external and internal leakages. 2014;27–42.

[15] Yi L, Changchuan X, Chao Y, Jialin C. Gust response analysis and wind tunnel test for a high-aspect ratio wing. Chin J Aeronaut. 2015;(December):1–8.

[16] Meile W, Ladinek T, Brenn G, Reppenhagen A, Fuchs A. Non-symmetric bi-stable flow around the Ahmed body. Int J Heat Fluid Flow. 2016;57:34–47.

[17] Sauder HS, Sarkar PP. Real-time prediction of aeroelastic loads of wind turbine blades in gusty and turbulent wind using an improved load model. Eng Struct. 2017;147:103–113.

[18] Rana K, Manzoor S, Sheikh NA, Ali M, Ali HM. Gust response of a rotating circular cylinder in the vortex suppression regime. Int J Heat Mass Transf. 2017;115:763–776.

[19] Zhan J, Xu B, Wu J, Wu J. Power extraction performance of a semi-activated flapping foil in gusty flow. J Bionic Eng. 2017;14(1):99–110.

[20] Bali K, Supradeepan K. Numerical analysis of flow past an oscillating circular cylinder using arbitrary Lagrangian Eulerian consistent flux reconstruction scheme. 2019;00(0):1–24.

[21] Joshi YA, Pandya D, Bhoraniya R, Harichandan AB. Numerical simulation of low Reynolds number gusty flow past two side-by-side circular cylinders. Lect Notes Mech Eng. 2021;29:71–78.

[22] Joshi YA, Bhoraniya R, Harichandan AB. Numerical analysis of incompressible low-Re impulse-flow over staggered 2D circular cylinders. Int J Eng Trends Technol. 2023;71(5):259–265.

[23] Gajula S, Bej N, Harichandan AB. Gust-induced flow perturbations on circular cylinder: Investigating the effects and characteristics. Int J Thermofluids. 2024;22(February):100607.

[24] Golubev VV, Nguyen L. High-accuracy low-Re simulations of airfoil-gust and airfoil-vortex interactions. 2010;(July):1–19.

[25] Wiesenberger VC. Neuere Festellungen über die Gesetze des Luftwiderstands. Phys Z. 1921;22:231.

[26] Tritton DJ. Experiments on the flow past a circular cylinder at low Reynolds numbers. J Fluid Mech. 1959;6(4):547–567.

[27] Gresho PM, Lee RL, Sani RC. On the time-dependent solution of the incompressible Navier-Stokes equations in two and three dimensions. Recent Adv Numer Methods Fluids. 1980;1:27–79.

[28] Roshko. On the drag and shedding frequency of two-dimensional bluff bodies. NACA Tech Note. 1954;(3169):1–30.

[29] Friehe CA. Vortex shedding from circular cylinders at low Reynolds numbers. J Fluid Mech. 1971;46(4):749–756.

[30] Braza M, Chassaing P, Ha Minh H. Numerical study and physical analysis of the pressure and velocity fields in the near wake of a circular cylinder. J Fluid Mech. 1986;165:79–130.

[31] Meneghini JR. Numerical simulation of flow interference between two circular cylinders in tandem and side-by-side arrangements. J Fluids Struct. 2001;15:327–350.

[32] Ding H, Shu C, Yeo KS, Xu D. Numerical simulation of flows around two circular cylinders by mesh-free least square-based finite difference methods. Int J Numer Methods Fluids. 2007;53:305–332.